Prudil and Welland *Materials Theory* (2017) 1:4
DOI 10.1186/s41313-017-0003-3

Materials Theory

ORIGINAL ARTICLE Open Access

A novel model of third phase inclusions on two phase boundaries

Andrew A. Prudil* and Michael J. Welland

* Correspondence:
Andrew.Prudil@cnl.ca
Fuel & Fuel Channel Safety Branch, Canadian Nuclear Laboratories, 286 Plant Rd, Chalk River, Ontario K0J 1J0, Canada

Abstract

A new computationally efficient model of an included phase located at the interface between two other phases is developed by projecting the boundaries of the inclusion onto the boundary between the two other phases. This reduces the 3D problem to one on a 2D surface while still being embedded in 3D space, which significantly reduces computational expense of solving the system. The resulting model is similar to conventional phase-field models. The properties of the solution are examined, compared to classical theory, and the numerical behaviour, including a mesh sensitivity analysis, are discussed. The model accurately captures mesoscale effects, such as the Gibbs-Thompson effect, coarsening, and coalescence. An example application of the model simulating the evolution of grain boundary porosity in nuclear fuel is shown on a representative tetrakaidecahedron-shaped fuel grain.

Keywords: Mesoscale, Interfaces, Phase-field

Background

The presence of an included phase on the interface between two other phases is a common phenomenon at multiple length scales. Some examples include vapour condensing on a solid, liquid flowing/beading on a solid, precipitation of inclusions at grain boundaries, surface films, and reactions on liquid-liquid boundaries. Contemporary diffuse interface modelling techniques are able to capture these three-phase phenomena robustly (Nestler et al. 2005; Choudhury et al. 2012; He et al. 2015; Chakraborty et al. 2014; Provatas et al. 2005; Li and Kim 2012; Ahmed et al. 2016; Rokkam et al. 2009). The minimisation of interfacial energy, typically implying the reduction of interface area, is a key driving force for the evolution of the composition and topology of these systems. The total energy of the system includes the integral of the local energy density over all of the interfaces. The chemical potential of a component is introduced, which is the partial variational derivative of the total energy with respect to the amount of that component. The mass flux in the system is assumed proportional to the gradient of this chemical potential, which evolves the system towards the local minimum energy.

In these methods, the diffuse interfaces are represented as volumes where the phase transitions continuously from one value to another. These real-space methods must therefore be 3D with spatial resolution on the order of the thickness of the diffuse interface in order to resolve interfaces/curvature effects correctly. Furthermore, in order to allow for mobility of these interfaces, and to resolve the physical conditions

leading to their evolution, the methods must resolve the volumes away from the interfaces to a similar resolution. The robustness of the diffuse interface models therefore comes at significant computational expense, which can be prohibitive for many 3D applications (Welland et al. 2015a). Some savings can be achieved for some models using adaptive solution techniques (i.e., h and/or p refinement), but the overall computational cost remains high, limiting model sizes and integration into multiphysics codes (Provatas et al. 2005; Li and Kim 2012).

In this work, a new computational method is proposed by which the geometry of phases included on a boundary is captured on the 2D interfaces between the phases within the 3D volume. Reduction of dimensionality results in substantial savings of computational expense, enabling faster computation times or consideration of larger system sizes. This is analogous to the use of beam or shell elements in structural mechanics to model the behaviour of high-aspect ratio components. As a consequence of the surface representation employed by the model, the technique is limited to contact angles of less than 90° and geometries that allow the interfaces to be mapped to a fixed computational domain. A contact angle of 90° is frequently considered a threshold for the wettability of a phase on an interface, an example of which being the convention of water on a surface being considered hydrophobic or hydrophilic. There are numerous cases of interest where the contact angle is less than 90° to which this model may be applied (He et al. 2015; Chakraborty et al. 2014). The cause and impact of the limitations of the model are discussed below.

The model is a conceptual combination of a classical sharp interface in one dimension and a Cahn-Hilliard phase-field model in the other two dimensions. It retains much of the robustness of the latter in handling complex interface morphologies including formation and coalescence of phases. The model can also incorporate the temporal and spatial dependence of the interfacial energies as may result from facet and state-dependent interfacial energies.

In the "Model formulation" section, the model is derived in its complete form and various possible simplifications are discussed. In the "Analysis of the model" section, the interface width, sharp interface limit, and contact angle error are examined. The numerical behaviour of a basic implementation is examined in the "Numerical behaviour" section, with respect to a mesh sensitivity analysis, parameter dependence, and recovery of the Gibbs-Thompson effect. Finally, an example application of the evolution of grain boundary porosity in nuclear fuel is shown in the "Example application to grain boundary porosity in nuclear fuel" section.

Model formulation

Consider a 2D surface embedded in 3D space, labelled X. We introduce a second surface, S, a non-negative distance away from X. Figure 1 shows a cross-section of such a scenario, where surfaces S and X represent phase boundaries between phases α, β, and γ. In this schematic, where S is apart from X, the surface S demarks the boundary between α and β and X demarks the boundary between β and γ. Where S coincides with X, the surfaces represent the same boundary between the α and γ phases.

The volume enclosed between S and X represents an included phase on X, as shown in Fig. 2. The intent is to calculate the evolution of the parameterised surface S on the computational domain X, thereby capturing the 3D interface between the three phase

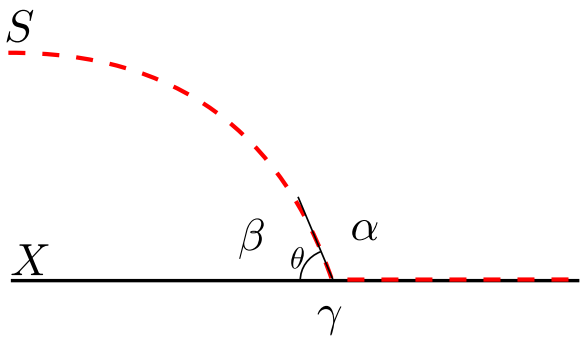

Fig. 1 Schematic of surfaces S and X separating phases *α*, *β*, and *γ*. The contact angle *θ* is also shown

boundaries on a single surface. The surface S can be represented as a parametrisation on the surface X. This is accomplished by transforming S onto X following a projection vector, $\vec{r}$, as depicted in Fig. 3. This projection vector is required to be smoothly varying everywhere on X, including any sharp edges and vertices and should be close to the local normal as discussed below.

In order to generate such a vector field for a closed surface, a suitable "focal point", $\vec{f}$, is selected towards which $\vec{r}$ is directed. The point $\vec{f}$ is usually, but is not necessarily required to be, selected as the centre of curvature of X. The selection of the point $\vec{f}$ does impose some limitations on the model which are discussed at the end of this section. Representing the current point on X as $\vec{x}$, the vector field is defined

$$\vec{r} = \vec{f} - \vec{x} = r\hat{r}, \tag{1}$$

where $\hat{r}$ is the unit direction vector of $\vec{r}$ and r is the magnitude of the $\vec{r}$ vector. The corresponding point on S, $\vec{s}$, is defined by the equation

$$\vec{s} = \vec{x} + h\hat{r}, \tag{2}$$

in which h is the unknown scalar variable calculated on X, which is the distance from surface X to surface S along the vector $\vec{r}$.

It should be noted that h may be positive or negative, representing surfaces above or below the surface of X relative to $\vec{f}$. In principle, it is possible to represent separate surfaces above and below surface X simultaneously leading to two values of h. However, in this work, a single surface S is considered that can be mirrored assuming symmetry above and below X.

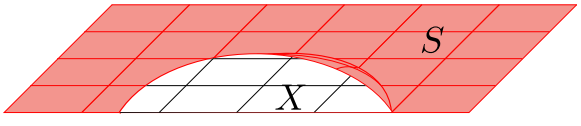

Fig. 2 Schematic of how a volume enclosed between S and X can represent a precipitated phase on X

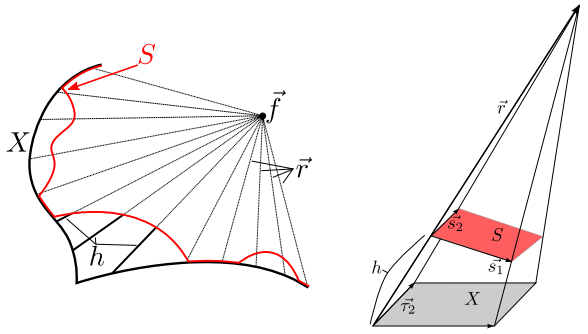

Fig. 3 Schematic of projection method, showing (*left*) selection of suitable focal point *X* and (*right*) labelled projection construct

The total interfacial energy of the system, E, is calculated as the integral of the interfacial energy density, σ, between phases (labelled by subscripts) and a possible triple junction energy,

$$\begin{aligned} E = &\int_{\mathrm{S}} \sigma_{\alpha\beta} dS + \int_{\mathrm{X}} \sigma_{\beta\gamma} dX \quad \text{where } \mathrm{S}\neq\mathrm{X} \\ &+ \int_{\mathrm{X}} \sigma_{\alpha\gamma} dX \quad \text{where } \mathrm{S} = \mathrm{X} \\ &+ \int_{\mathrm{L}} \sigma_{\alpha\beta\gamma} dL \end{aligned} \tag{3}$$

where dS is an infinitesimal area of surface S and dX is an infinitesimal area of surface X, and dL is an infinitesimal line segment between S and X corresponding to the triple junction. In general, externally imposed forces, such as gravity and aerodynamic drag, may be introduced in Eq. 3 as additional system potentials; however, these are neglected from the current derivation for the sake of simplicity.

Since the surface S is defined parametrically in terms of the computational domain, the relation between the area elements of S and X is

$$dS = \left|\overrightarrow{s_1} \times \overrightarrow{s_2}\right| dX, \tag{4}$$

where the vectors $\overrightarrow{s_1}$ and $\overrightarrow{s_2}$ are the gradients of surface S on X corresponding to the unit surface tangent vectors $\hat{\tau}_1$ and $\hat{\tau}_2$ at point $\overrightarrow{x}$, as shown in Fig. 3. The figure shows orthogonal tangent vectors, although the following derivation does not require such. Denoting the spatial derivatives in the local coordinates along these vectors with the subscripts τ_1 and τ_2, $\overrightarrow{s_1}$ and $\overrightarrow{s_2}$ may be calculated and expressed as,

$$\overrightarrow{s_1} = (\hat{\tau}_1 \cdot \nabla)\overrightarrow{s} = \hat{\tau}_1 + h_{\tau_1}\hat{r} + h\hat{r}_{\tau_1}, \tag{5}$$

$$\overrightarrow{s_2} = (\hat{\tau}_2 \cdot \nabla)\overrightarrow{s} = \hat{\tau}_2 + h_{\tau_2}\hat{r} + h\hat{r}_{\tau_2}. \tag{6}$$

In order to perform the integral over the whole domain while distinguishing between "S ≠ X" and "S = X", a phase function, $p(h)$, is defined that varies between 0 and 1, corresponding to where S is in contact with X, as determined by the local value of h. This

scheme is illustrated in Fig. 4 which shows the range of h in which p varies from 1 to 0, and the resulting diffuse interface of width d. This interface is treated as being spatially diffuse, similar to standard phase-field models that demonstrate robustness and versatility of handling complex interface morphology (Cahn and Hilliard 1958). Due to the spatial variation of h as the dependant variable, this implies $p(h)$ be diffuse in h, between $h = 0$, representing the coincidence of S and X, and $h > h'$, representing the separation of S and X. The value of h' is user-defined transition size and linked to the choice of the form of $p(h)$. The region $0 > h > h'$ therefore denotes the diffuse triple junction interface between the three phases.

It should be noted that the model of the included phase is sharp across the surface S which has no associated thickness. The diffuse interface occurs where S meets X, over a user-defined transition size in h and therefore an interval in space. This region also defines the $\alpha - \beta - \gamma$ triple junction which is therefore partially diffuse. Since it is here that the contact angle is defined, the user-defined transition size impacts the contact angle observed in the model. In the "Stationary point" section, we demonstrate that in the limit of zero transition size, the sharp interface contact angle is recovered. In the "Contact angle" section, we further demonstrate that the results of the numerical model converge towards the sharp interface when the transition size is decreased.

The form of $p(h)$ is flexible as long as the following conditions are respected:

$$p(h = 0) = 0, \tag{7}$$

$$p(h = h') = 1, \tag{8}$$

$$\frac{\partial p}{\partial h}(h = 0) = \frac{\partial p}{\partial h}(h = h') = 0, \tag{9}$$

such that both phases at equilibrium are locally stable with respect to variations in h. A particular example of $p(h)$ is shown in the "Numerical behaviour" section, but the properties of the model can be derived regardless of this choice.

Triple junction energy can be added to the model, which only occurs within the diffuse interface. A function $g(p)$ is introduced, with the requirement that $g(p = 0) = g(p = 1) = 0$ and $\frac{\partial g}{\partial p}(p = 0) = \frac{\partial g}{\partial p}(p = 1) = 0$. Once more, the form of this function is flexible, but a standard double well potential, $g \propto p^2(1 - p)^2$, may be used.

Utilising the phase function and the interface energy densities with subscripts according to the phases, the energy functional becomes

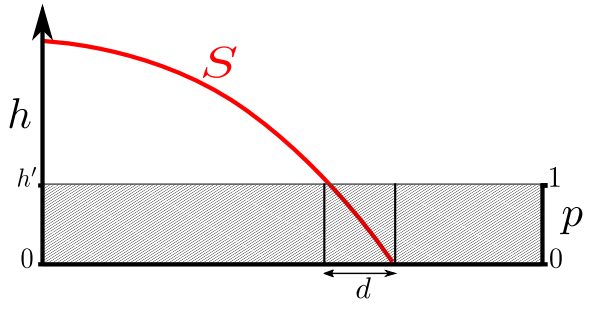

Fig. 4 Schematic of how the diffuse interface is captured as p varies from 0 to 1, and the associated diffuse interface width, d

$$E = \int_X \left(p\left[\sigma_{\alpha\beta}\left|\overrightarrow{s_1} \times \overrightarrow{s_2}\right| + \sigma_{\beta\gamma}\right] + \sigma_{\alpha\gamma}[1-p] + \sigma_{\alpha\beta\gamma}g(p)\right)dX, \tag{10}$$

which describes the energy of the system in terms of the areas of the three interfaces. Suppose now that the volume enclosed between S and X represents the precipitated (β) phase, consisting of a mobile species with concentration c. Assuming constant density ρ, the concentration of the species is related to the volume by $c = \rho V$. The chemical potential of this species, μ, is defined as the functional derivative with respect to the concentration

$$\mu = \frac{\delta E}{\delta c} = \frac{1}{\rho}\frac{\delta E}{\delta h}\frac{\delta h}{\delta V}. \tag{11}$$

which necessitates calculating the variational derivative of volume enclosed by h.

Consider the area elements as the bases of pyramids with apex $\overrightarrow{f}$, as shown in Fig. 3. The volume is calculated as one third the base times the perpendicular height, which is the projection of the normal vector of X, $\hat{n}$, onto $\overrightarrow{r}$. The enclosed volume is therefore the difference between pyramids defined by X and S, and the volume is

$$V = \int_X \frac{r}{3}\left(\left[\hat{n} - \left(\overrightarrow{s_1} \times \overrightarrow{s_2}\right)\left(1-\frac{h}{r}\right)\right]\cdot\hat{r}\right)dX. \tag{12}$$

The functional derivative of Eq. 12 is evaluated by the Euler-Lagrange equation

$$\frac{\delta V}{\delta h} = \left(\frac{\partial}{\partial h} - \frac{\partial}{\partial \hat{\tau}_1}\frac{\partial}{\partial h_{\tau_1}} - \frac{\partial}{\partial \hat{\tau}_2}\frac{\partial}{\partial h_{\tau_2}}\right)\left(\frac{dV}{dA}\right). \tag{13}$$

The last two terms in the first parenthesis on the right-hand side consist of the derivatives with respect to the gradient in h. They are found to be zero utilising $\overrightarrow{s_1}$ and $\overrightarrow{s_2}$ defined by Eq. 5 and 6, respectively, and noting that the triple product $\left(\overrightarrow{a} \times \overrightarrow{b}\right)\cdot\overrightarrow{a} = 0$ is for all $\overrightarrow{a}$ and $\overrightarrow{b}$. Additionally, it can be shown that for pyramids, the area of any cross-section scales according to the square of the fractional height, and therefore (Harris and Stöcker 1998),

$$\overrightarrow{s_i}(h, \nabla h) = \left(1-\frac{h}{r}\right)\overrightarrow{s_i}(h = 0, \nabla h), \tag{14}$$

Therefore, one can write

$$\frac{\partial}{\partial h_{\tau_1}}\left(\left(\overrightarrow{s_2} \times \overrightarrow{s_2}\right)\cdot\overrightarrow{r}\right) = \left(\hat{r} \times \overrightarrow{s_2}\right)\cdot\overrightarrow{r} = 0, \tag{15}$$

$$\frac{\partial}{\partial h_{\tau_2}}\left(\left(\overrightarrow{s_1} \times \overrightarrow{s_2}\right)\cdot\overrightarrow{r}\right) = \left(\overrightarrow{s_1} \times \hat{r}\right)\cdot\overrightarrow{r} = 0, \tag{16}$$

$$\frac{\partial\left(\overrightarrow{s_1} \times \overrightarrow{s_2}\right)}{\partial h} = -\frac{2}{r}\left(1-\frac{h}{r}\right)^{-1}\left(\overrightarrow{s_1} \times \overrightarrow{s_2}\right), \tag{17}$$

which, when simplified, yields the intuitive answer for Eq. 13,

$$\frac{\delta V}{\delta h} = \left(\overrightarrow{s_1} \times \overrightarrow{s_2}\right) \cdot \hat{r}. \tag{18}$$

The variational derivative of the energy functional with respect to the variable h must also be evaluated using the Euler-Lagrange equation. Noting that in general, the phase function depends only on h, while $\overrightarrow{s_1}$ and $\overrightarrow{s_2}$ depends on both h and ∇h, $\frac{\delta E}{\delta h}$ becomes

$$\frac{\delta E}{\delta h} = \left(\sigma_{\alpha\beta}\left|\overrightarrow{s_1} \times \overrightarrow{s_2}\right| + \sigma_{\beta\gamma} - \sigma_{\alpha\gamma} + \sigma_{\alpha\beta\gamma}\frac{\partial g}{\partial p}\right)\frac{\partial p}{\partial h}$$

$$+ p\sigma_{\alpha\beta}\frac{\partial\left|\overrightarrow{s_1} \times \overrightarrow{s_2}\right|}{\partial h} - \sigma_{\alpha\beta}\left(\frac{\partial}{\partial \hat{\tau}_1} p \frac{\partial\left|\overrightarrow{s_1} \times \overrightarrow{s_2}\right|}{\partial h_{\tau_1}} + \frac{\partial}{\partial \hat{\tau}_2}, p\frac{\partial\left|\overrightarrow{s_1} \times \overrightarrow{s_2}\right|}{\partial h_{\tau_2}}\right), \tag{19}$$

which can be further simplified utilising Eqs. 5, 6, and 17 to obtain a form suitable for implementation in computer codes

$$\frac{\delta E}{\delta h} = \left(\sigma_{\alpha\beta}|\overrightarrow{s_1} \times \overrightarrow{s_2}| + \sigma_{\beta\gamma} - \sigma_{\alpha\gamma} + \sigma_{\alpha\beta\gamma}\frac{\partial g}{\partial p}\right)\frac{\partial p}{\partial h} - p\sigma_{\alpha\beta}\frac{2}{r}\left(1 - \frac{h}{r}\right)^{-1}|\overrightarrow{s_1} \times \overrightarrow{s_2}| \tag{20}$$

$$-\sigma_{\alpha\beta}\left(\frac{\partial}{\partial \hat{\tau}_1} p \frac{\overrightarrow{s_1} \times \overrightarrow{s_2}}{\left|\overrightarrow{s_1} \times \overrightarrow{s_2}\right|} \cdot \hat{r} \times \overrightarrow{s_2} + \frac{\partial}{\partial \hat{\tau}_2} p \frac{\overrightarrow{s_1} \times \overrightarrow{s_2}}{\left|\overrightarrow{s_1} \times \overrightarrow{s_2}\right|} \cdot \overrightarrow{s_1} \times \hat{r}\right).$$

This can be used to evaluate the chemical potential of the included phase by Eq. 11. Note that the term $\frac{\overrightarrow{s_1} \times \overrightarrow{s_2}}{\left|\overrightarrow{s_1} \times \overrightarrow{s_2}\right|} = \hat{n}_S$, the unit normal to the interface.

The gradient in the chemical potential is the driving force for the mass flux, J. The mass flux may apply to a layer along the interface S, in the case of surface diffusion or as an approximation to bulk diffusion, or the enclosed volume, such as vapour phase transport. In general, surface, bulk, and volume diffusion occur, but one of them usually dominates for any specific situation (Welland 2012).

In order for this to be a reasonable approximation for volume diffusion, the gradient of μ along $\hat{r}$ must be small relative to the gradient along surface tangent vectors $\overrightarrow{\tau_1}$ and $\widehat{\tau_2}$, such as when the thickness of the included phase is small compared to the characteristic length scale along X (i.e. when $h \ll r$). Using the notation $\nabla_\tau = \frac{\partial}{\partial \tau_1}, \frac{\partial}{\partial \tau_2}$, the net flux acting on the volume, J_V, is

$$J_V = \rho V M_V\left[-\nabla_\tau \mu + \overrightarrow{F_V}\right], \tag{21}$$

where $\overrightarrow{F_V}$ is a generic external force and M_V is the mobility through the volume, related to the diffusion coefficient, D, by $M_V = \frac{D}{RT}$ for an ideal solution where RT is the ideal gas constant times the absolute temperature (Welland et al. 2014). Similarly, the net mass flux from surface phenomena, J_S, represented on X is

$$J_S = \rho\left|\overrightarrow{s_1} \times \overrightarrow{s_2}\right| T_{int} M_S\left[-\nabla_S \mu + \overrightarrow{F_S}\right]. \tag{22}$$

Here, the volume is replaced with the surface area, $\left|\overrightarrow{s_1} \times \overrightarrow{s_2}\right|$, times the effective thickness of the interface, T_{int}. M_S is the surface mobility, which for practical purposes can be combined with the thickness into a single effective material property, $\frac{D_{S\text{eff}}}{RT} = T_{int} M_S$. The variable $\overrightarrow{F_S}$ accounts for surface forces, which may be present, such as drag or friction. The

gradient along the surface, ∇_S, can be expressed in terms of ∇_τ, using the transformation matrix $[\boldsymbol{T}]$ that accounts for the change in path length along each coordinate akin to the arbitrary Lagrangian-Eulerian method (Donea et al. 2004),

$$\nabla_S = [\boldsymbol{T}]\nabla_\tau. \tag{23}$$

The overall mass conservation equation for concentration of the beta phase, assuming constant density as in Eq. 11, including both surface and volume fluxes, as well as a source term, Q, becomes

$$\frac{\partial c}{\partial t} = \rho \frac{\delta V}{\delta h}\frac{\partial h}{\partial t} = -\nabla_\tau \cdot J_V + -\nabla_S \cdot J_S + Q. \tag{24}$$

The model therefore requires the solution of the partial differential equation for Eq. 24 with the chemical potential from Eq. 11, the variation of volume with h from Eq. 18, and the variation in total energy with h from Eq. 20. When combined, this is a fourth order non-linear partial differential equation for h, defined on the 2D surface X. Alternately, Eq. 11 may be solved simultaneously with Eq. 24 for μ and h as two coupled second order equations on X. This allows it to be solved using the standard C_0 continuous Lagrange elements available in most finite-element method codes. Note that although the equations are in terms of the distances between surfaces h, the conserved quantity is still the concentration of the β phase c. This is also equivalent to conservation of the volume of the β phase since density has been assumed constant in this version of the model.

The suitability criteria for the vector field $\overrightarrow{r}$ and the selection of the focal point $\overrightarrow{f}$ can now specified. Considering Fig. 3, it is clear that in order for S to be uniquely defined, there must be a one-to-one mapping from X to S. Specifically, $\hat{n}_S \cdot \hat{r} \neq 0$, for *all* points on X. From this requirement, the contact angle of the included phase with respect to surface X must be less than the minimum value of $\sin^{-1}(\hat{n}_X \cdot \hat{r})$ over the domain. This is the reason that contact angles equal to or greater than 90° are not representable in this work in the ideal case where $\hat{r} = \hat{n}_X$. For practical geometries where $\hat{n}_X \cdot \hat{r} < 1$, such as along edges between facets, this limits the contact angle to less than half the internal angle. By careful definition of $\hat{r}$, the limitations imposed by this requirement can be minimised. Note that this does not preclude concave surfaces nor does it preclude complex 2D manifolds.

Thin interface approximation

In the case where $\overrightarrow{f}$ may be far enough from X such that $r \gg h$, the spatial variation of $\hat{r}$ can be neglected. Under this approximation, Eqs. 5 and 6 become

$$\overrightarrow{s_1} = \widehat{\tau_1} + h_{\tau_1}\hat{r}, \tag{25}$$

$$\overrightarrow{s_2} = \widehat{\tau_2} + h_{\tau_2}\hat{r}. \tag{26}$$

One can also simplify Eq. *12* to read

$$V = \int_X \hat{n} \cdot h\hat{r}\, dX, \tag{27}$$

and therefore,

$$\frac{\delta V}{\delta h} = \hat{n} \cdot \hat{r}, \tag{28}$$

which avoids the multiple calculations of the cross product, $\overrightarrow{s_1} \times \overrightarrow{s_2}$, and their derivatives, leading to significant computational savings.

Special case of flat interfaces

A further simplification is possible when $\hat{r} \approx \hat{n}$ (e.g. a planer or spherical geometry), such that Eqs. 5 and 6 become

$$\overrightarrow{s_1} = \widehat{\tau_1} + h_{\tau_1} \hat{n}, \tag{29}$$

$$\overrightarrow{s_2} = \widehat{\tau_2} + h_{\tau_2} \hat{n}. \tag{30}$$

and leads to a simplified form for the cross-products, in the tangent system,

$$\overrightarrow{s_1} \times \overrightarrow{s_2} = \langle -h_{\tau_1}, -h_{\tau_2}, 1 \rangle, \tag{31}$$

$$\left| \overrightarrow{s_1} \times \overrightarrow{s_2} \right| = \sqrt{1 + h_{\tau_1}^2 + h_{\tau_2}^2}. \tag{32}$$

Additionally, for the planar case, one simplifies Eq. *28* to

$$\frac{\delta V}{\delta h} = 1. \tag{33}$$

The mass balance in Eq. 24 therefore becomes

$$\rho \frac{\partial h}{\partial t} = -\nabla_\tau \cdot J_V + -\nabla_S \cdot J_S + Q, \tag{34}$$

and the chemical potential becomes

$$\mu = \frac{1}{\rho} \frac{\delta E}{\delta h} = \frac{1}{\rho} \left(\sigma_{\alpha\beta} \sqrt{1 + h_{\tau_1}^2 + h_{\tau_2}^2} + \sigma_{\beta\gamma} - \sigma_{\alpha\gamma} + \sigma_{\alpha\beta\gamma} \frac{\partial g}{\partial p} \right) \frac{\partial p}{\partial h} - \frac{1}{\rho} \nabla_\tau \cdot \frac{p \sigma_{\alpha\beta} \nabla_\tau h}{\sqrt{1 + h_{\tau_1}^2 + h_{\tau_2}^2}}. \tag{35}$$

The mass-flux equations remain largely unchanged except for the simplified volume in Eq. 21.

Analysis of the model

The properties of the solution to the 1D problem with the flat interface discussed in the "Special case of flat interfaces" section is now examined. Figure 5 shows an example of an expected solution in the neighbourhood of the interface shown in Fig. 1, showing approximately straight h profiles on either side of the interface, with a simulated contact angle ϕ.

Condition far from the interface

As depicted in Fig. 5, the profile of h and p may have a non-zero minima, h^∞ and p^∞, away from the interface. This is for the general case in phases of small radii to increase the solubility of the included species in the surrounding material (Lupis 1983; Welland et al. 2015b). Here, the surface S is flat and parallel to X. For geometries of reasonable size $h^\infty \ll r$, in which case, $\overrightarrow{s_1} \times \overrightarrow{s_2} = dA\, \hat{n}$. The chemical potential from Eq. 11 is therefore

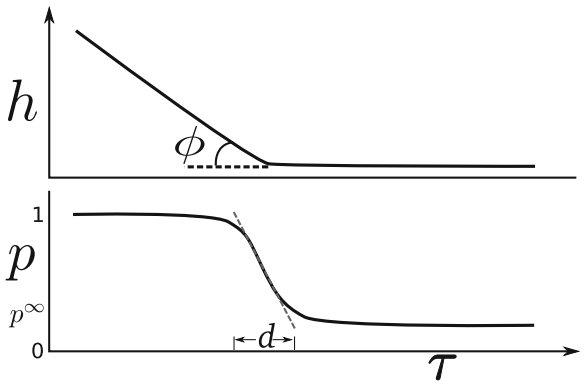

Fig. 5 Expected solution of the system in the neighbourhood of the interface showing (*top*) the expected profile of h with the simulated contact angle φ and (bottom) the expected profile of p varying between p^{∞} and 1 over an interface width, d

$$\mu = \frac{1}{\rho}\left(\sigma_{\alpha\beta} + \sigma_{\beta\gamma} - \sigma_{\alpha\gamma} + \sigma_{\alpha\beta\gamma}\frac{\partial g}{\partial p}\Big|_{p^{\infty}}\right)\frac{\partial p}{\partial h}\Big|_{h^{\infty}}. \tag{36}$$

The chemical potential far from the interface is therefore determined completely by the interfacial energies, p^{∞}, and the form of $p(h)$. In the "Comparison against the Gibbs-Thompson effect" section, the model numerical predictions will be compared against the classical Gibbs-Thompson relation.

Interface width

An approximation of the interface width can be calculated knowing that $p(h)$ varies from ~0 to ~1 across the interface. Following the method established by Cahn and Hilliard (Cahn and Hilliard 1958), the interface width can be characterised

$$d \approx \frac{1}{\max\frac{\partial p}{\partial \tau}} = \left(\max\frac{\partial p}{\partial h}h_{\tau}\right)^{-1}. \tag{37}$$

The interface width thus depends on the form of $p(h)$ and is inversely proportional to $\frac{\partial p}{\partial h}$.

For symmetric phase functions, $\max\frac{\partial p}{\partial h}$ typically occurs at $p \approx 0.5$. For this point, an approximate value of $h_{\tau}(p = 0.5)$ can be obtained as the average of the values at $h_{\tau}(p = 0) = 0$ and $h_{\tau}(p = 1) = \tan\theta$, such that $h_{\tau}(p = 0.5) \approx \frac{\tan\theta}{2}$. An approximate interface width is therefore

$$d \approx \frac{2}{\tan\theta}\left(\frac{\partial p}{\partial h}\Big|_{p=0.5}\right)^{-1}. \tag{38}$$

This approximation will be shown to be appropriate in the "Contact angle" section.

Stationary point

The solution depicted in Fig. 5 represents a minimum in the energy functional in Eq. 10, subject to a constraint of mass conservation. This statement is equivalent to asserting a constant chemical potential everywhere in the system. Disregarding generalised body forces, which may be position dependant, the energy functional in Eq. 10 does

not explicitly depend on the spatial coordinates, and therefore, the Beltrami identity may be used to obtain the stationary points of the Euler-Lagrange equation. For a functional with integrand L, the identity is

$$L - \nabla u \cdot \frac{\partial L}{\partial \nabla u} = c_0 \tag{39}$$

where c_0 is a constant. Applying this to the functional in Eq. 10, noting that $\left|\overrightarrow{s_1} \times \overrightarrow{s_2}\right| = \sqrt{1 + h_\tau^2}$ in 1D, and simplifying,

$$p\left[\frac{\sigma_{\alpha\beta}}{\sqrt{1 + h_\tau^2}} + \sigma_{\beta\gamma} - \sigma_{\alpha\gamma}\right] + \sigma_{\alpha\gamma} + g^\infty \sigma_{\alpha\beta\gamma} = c_0. \tag{40}$$

Considering the solution far from the interface between the α and γ phases, h approaches a constant, and h_τ approaches 0. The constant c_0 is therefore

$$c_0 = p^\infty \left[\sigma_{\alpha\beta} + \sigma_{\beta\gamma} - \sigma_{\alpha\gamma}\right] + \sigma_{\alpha\gamma} + g^\infty \sigma_{\alpha\beta\gamma}. \tag{41}$$

In order to relate this to the contact angle, the tangential derivative of h may be written in terms of the contact angle with respect to the surface X, ϕ (i.e. $h_\tau = \tan\phi$), and use the trigonometric identity $\cos\phi = \frac{1}{\sqrt{1+\tan^2\phi}}$,

$$p\left[\sigma_{\alpha\beta}\cos\phi + \sigma_{\beta\gamma} - \sigma_{\alpha\gamma}\right] + g\sigma_{\alpha\beta\gamma} = p^\infty \left[\sigma_{\alpha\beta} + \sigma_{\beta\gamma} - \sigma_{\alpha\gamma}\right] + g^\infty \sigma_{\alpha\beta\gamma}. \tag{42}$$

The sharp interface limit may be examined where the interface width approaches zero ($d \to 0$). Through Eq. 37, one finds that the sharp interface occurs when $\frac{\partial p}{\partial h} \to \infty$, which corresponds to $p(h)$ being a step function centred at $h = 0$. The step function requires $p^\infty = 0$ away from the interface, since it cannot take on an intermediate value, while inside the inclusion $p = 1$, which implies $g = 0$. Young's equation for a planer geometry is therefore recovered, such that the simulated angle ϕ is equal to the contact angle θ,

$$\sigma_{\alpha\beta}\cos\theta + \sigma_{\beta\gamma} - \sigma_{\alpha\gamma} = 0. \tag{43}$$

In general, the phase function is continuous and p^∞ is non-zero. Then, $p \geq p^\infty$ everywhere and

$$\cos\phi = \frac{p^\infty \left[\sigma_{\alpha\beta} + \sigma_{\beta\gamma} - \sigma_{\alpha\gamma}\right] + \left[g^\infty - g\right]\sigma_{\alpha\beta\gamma}}{p\sigma_{\alpha\beta}} - \frac{\sigma_{\beta\gamma} - \sigma_{\alpha\gamma}}{\sigma_{\alpha\beta}}. \tag{44}$$

and if the triple junction contribution is small,

$$\cos\phi = \frac{p^\infty}{p} + \left(\frac{p^\infty}{p} - 1\right)\frac{\sigma_{\beta\gamma} - \sigma_{\alpha\gamma}}{\sigma_{\alpha\beta}}. \tag{45}$$

Combining Eq. 43 with Eq. 44,

$$p\left[\cos\phi - \cos\theta\right] = p^\infty\left[1 - \cos\theta\right] + \left[g^\infty - g\right]\frac{\sigma_{\alpha\beta\gamma}}{\sigma_{\alpha\beta}}. \tag{46}$$

Inside the inclusion region, $p = 1$ and Eq. 46 may be approximated as

$$\theta - \phi = \frac{p^{\infty}[1-\cos\theta] + g^{\infty}\frac{\sigma_{\alpha\beta\gamma}}{\sigma_{\alpha\beta}}}{\sin\theta}. \tag{47}$$

Since $0° < \theta < 90°$, we expect $\theta > \phi$ in all cases.

Numerical behaviour

In order to demonstrate and analyse the performance of the model, it is compared to an analytic sharp interface solution representing a 1D azimuthally symmetric geometry in polar coordinates of a precipitate on an interface reflected on surface X. In this case, the segment in Fig. 1 where S is apart from X, corresponding to the β – γ interface is the computational bisection of the precipitate and does not constitute a real interface and therefore $\sigma_{\beta\gamma} = 0$.

The form of $p(h)$ is selected and parameterised by a transition size in h, symbolised as a. A finite transition thickness is selected because it is numerically difficult to implement p as a discontinuous step function. The thickness of the transition region is an input parameter that may be related to the finite dimension of the α-β-γ junctions or considered strictly computational in nature. A suitable form of the phase function based on a smoothed step function was chosen for its symmetry and smoothness,

$$p(h) = \begin{cases} \left(\frac{h}{a}\right)^3 \left(6\left(\frac{h}{a}\right)^2 - 15\left(\frac{h}{a}\right) + 10\right) & 0 \le h < a \\ 1 & h \ge a \end{cases}. \tag{48}$$

The interface width may now be calculated via Eq. 38,

$$d \approx \frac{2a}{\tan\theta}. \tag{49}$$

The model was implemented in COMSOL Multiphysics 5.2a using user-defined weak form equations and solved numerical with first order Lagrange elements for both the chemical potential and the displacement from the surface.

Contact angle

The contact angle of an inclusion on a flat surface according to the sharp interface theory is given by Young's equation,

$$\cos(2\theta) = \frac{\sigma_{\alpha\gamma}}{2\sigma_{\alpha\beta}} \tag{50}$$

A parameter sweep was conducted in which bubbles with an initial projected radius of 5 μm were initialized on a 10 μm domain and permitted to evolve to their equilibrium shapes for surface energy ratios of $\sigma_{\alpha\gamma}/\sigma_{\alpha\beta} = 0.174$ to 1.9696, corresponding to theoretical angles of 10° to 85°, and transition sizes of $a = 0.05$ to 0.3 μm, respectively. As discussed in the "Stationary point" section, one would expect to recover the sharp interface limit in the limit of zero transition size.

The 1D model allows an extremely fine finite-element mesh size of 1 nm to be created to eliminate potential effects of discretization error. A mesh sensitivity study was conducted separately in the "Mesh sensitivity study" section to investigate this issue. The simulated equilibrium geometries are shown in Fig. 6 for the 0.3 and 0.05 μm transition sizes. As expected, the impact of the transition size is visible at the edge of the bubble (i.e. $r \approx 0.5$ μm) in which the 0.3 μm transition size produces a much smoother

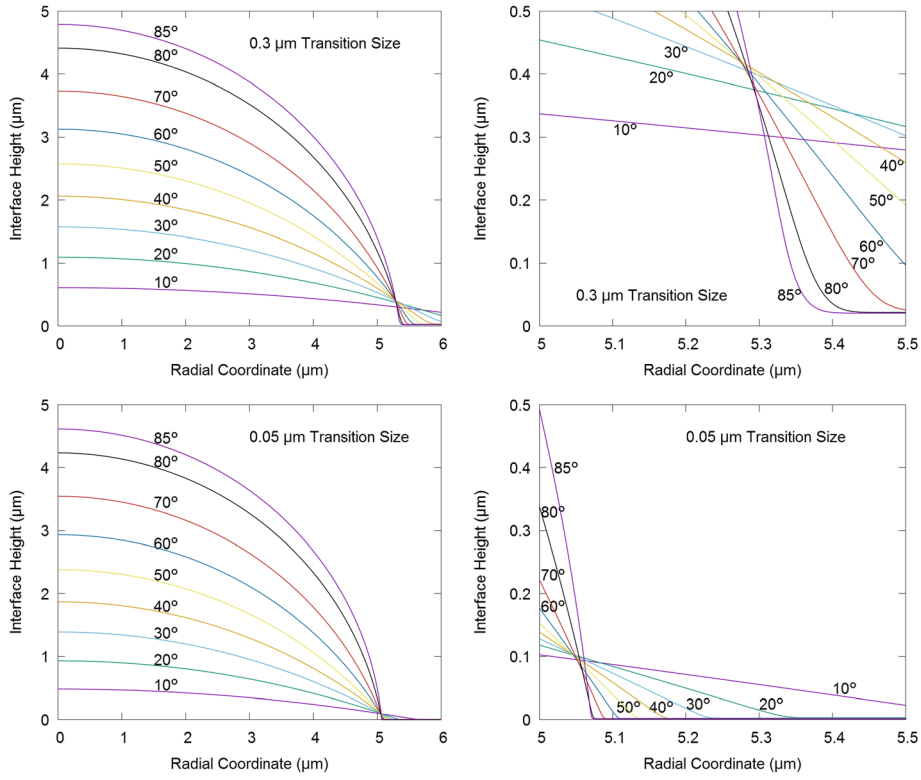

Fig. 6 Simulated bubble cross-sections for surface energies corresponding to sharp interface angles of 10° to 85° for transition size of 0.3 μm (*top left*) and 0.05 μm (*bottom left*), with enlarged triple junction regions (*top right* and *bottom right*, respectively)

corner compared to the 0.05 μm transition size. As a result of the smoother transition, the interface width is visibly larger for the 0.3 μm case. According to Eq. 49, the approximate interface widths for 85° should be $d_{0.3\ \mu m} = 0.0529$ μm and $d_{0.05\ \mu m} = 0.0088$ μm, which is roughly consistent with the observed smoothed region.

The simulated contact angle, ϕ, was calculated using two different techniques for comparison purposes. The first technique performs this calculation directly by finding the gradient of the bubble shape and converting it to an angle relative to the horizontal via inverse tangent function. The post-processing of this method is simple since the minimum gradient in the model occurs at the edge of the bubble and can therefore be found as the minimum on the finite-element domain, $\phi = \mathrm{atan}(\min(h_{\mathrm{tau}}))$.

The angle calculated by this method is presented in Fig. 7. The results indicate a clear trend converging towards the theoretical sharp interface angle θ as the transition size decreases for the whole range of angles, as expected. The difference between the angle observed in the simulations and the sharp interface prediction generally increases with the angle for large transition sizes; however, this trend diminishes as the transition size is decreased such that it becomes negligible for the 0.1 and 0.05 μm transition sizes.

As seen in Fig. 6, the finite interface thickness smooths the corner of the bubble, thereby reducing the angle calculated by this method. Although this provides a good measure of the sharpness of the interface, it does not indicate if the curvature is behaving as expected in the bulk material. In order to avoid this difficulty, the second method calculates the expected contact angle based on the values away from the transition region assuming the geometry in

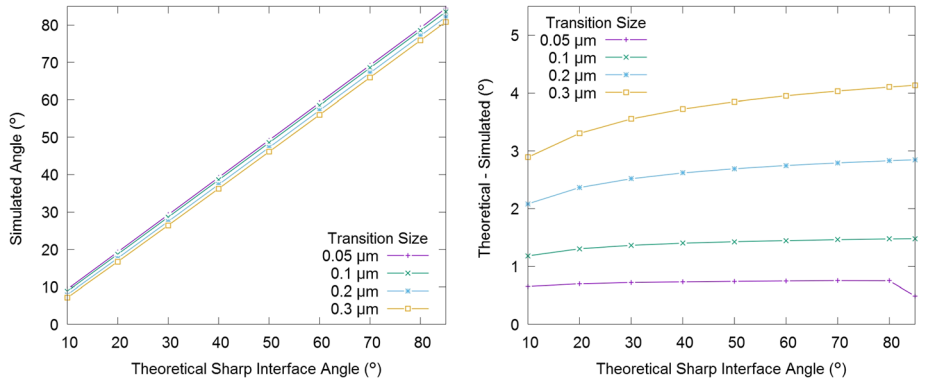

Fig. 7 *Left*: plot of contact angles calculated from gradient of simulation as a function of the theoretical sharp interface angle for the transition sizes between 0.05 and 0.3 μm. *Right*: the difference between the theoretical and simulated contact angles from the figure to the left

Fig. 8. Due to symmetry, the centre of the sphere defining the boundary of the bubble is located along the axis of symmetry (i.e. $r = 0$) displaced below the origin a distance Z_0. The contact angle can be found done using the bubble height at the origin, h_0, and the height at any other location on the sphere, $h(r)$. Using this methodology, the intersection angle of this sphere with the $h = 0$ axis can be calculated according to

$$Z_0 = \frac{r^2 + (h(r))^2 + (h_0)^2}{2(h(r) - h_0)}, \tag{51}$$

$$\theta = \operatorname{acos}\left(\frac{Z_0}{h_0 + Z_0}\right). \tag{52}$$

Since this is valid for all points on the β phase in the model, the average value is utilised to reduce numerical noise and obtain a single value for comparison. Note that this

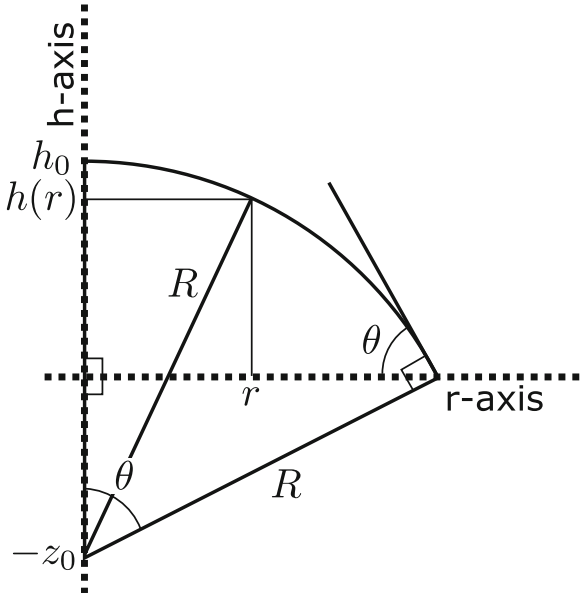

Fig. 8 Geometry for calculating the contact angle from two points on the surface

method is complimentary to the gradient-based method, since it is not calculating the contact angle actually observed in the model, but rather, it calculates the equivalent contact angle for a sphere of the same radius of curvature and location.

The contact angles calculated via this method is shown in Fig. 9 (left) for the same set of simulation results from Fig. 6. This second method shows better agreement with the theoretical values since it is less sensitive to smoothing of the edges in the transition zone. The error relative to the sharp interface limit is shown in Fig. 9 (right). These results also show a clear trend of converging towards the sharp interface limit as the transition size is decreased, which is in agreement with Eq. 48.

The simulated contact angle underpredicts the theoretical angle for all of the simulations in the sweep as a function of the transition size as expected by Eq. 47. The magnitude of the error observed is relatively small, roughly one third of the magnitude of the error calculated at the edge of the bubble, and can be managed via transition size and triple junction energy.

Mesh sensitivity study

It is necessary to develop an understanding of the meshing requirements in order to make efficient use of the model. To this end, a mesh sensitivity study was conducted for a fixed transition size of $a = 0.1$ μm and mesh density ranging from 0.1 to 100 mesh elements per transition size (i.e. a unitless dimension) for contact angles of 10° to 85°. Following the same procedure from the "Contact angle" section, the effective contact angle from the simulation was calculated using both the minimum gradient at the αβγ-triple junction method and the radius of curvature from the bulk αβ-interface method. These results are presented in Figs. 10 and 11, respectively. For all angles, it is observed that significant mesh dependence (i.e. non-converged values) results from excessively coarse meshes. For a sufficiently small mesh size, mesh sensitivity becomes small and the results converge a value close to the sharp interface limit.

Equation 49 has been superimposed on the simulation results assuming that the interface width (d) is equal to the mesh size (equivalent to having one mesh element per interface width). As expected, the threshold mesh size required for a converged

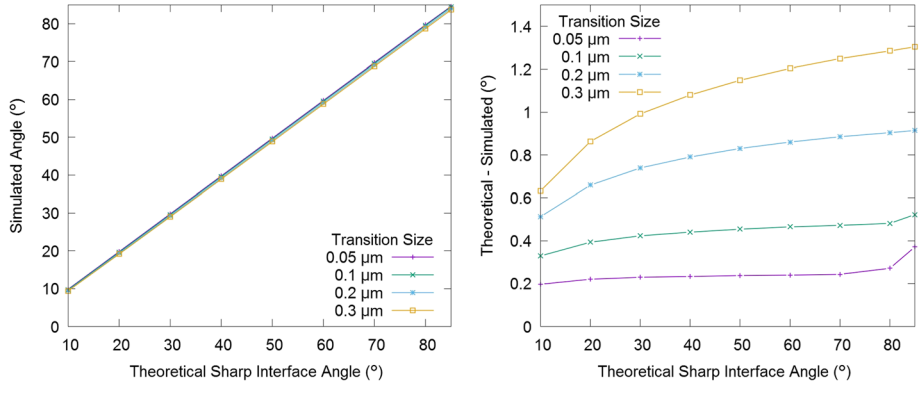

Fig. 9 *Left*: plot of contact angles calculated from the two-point method as a function of the theoretical sharp interface angle for the transition sizes between 0.05 and 0.3 μm. *Right*: difference between the theoretical and simulated contact angles from the figure to the left

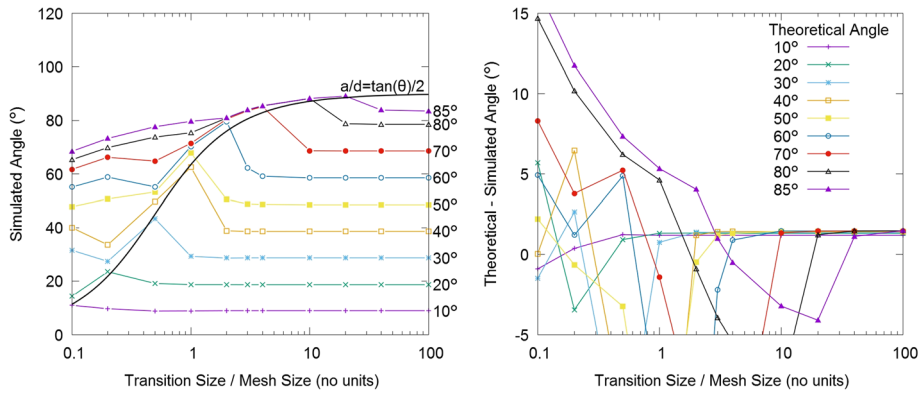

Fig. 10 *Left*: plot of contact angles calculated via the gradient method as a function of the mesh density and theoretical sharp interface contact angles for a transition size of 0.1 μm. *Right*: difference between the theoretical and simulated contact angles from the figure to the left

solution appears to be roughly proportional to this prediction, plus some additional mesh density for the larger contact angles to compensate for the numerical difficulty associated with large gradients.

Similar to the results from the transition size study, the mesh sensitivity calculated from the radius of curvature method demonstrates comparatively smaller error measurements and smoother convergence. Once again, more mesh sensitivity is observed at higher contact angles.

Overall, the results suggest that efficient meshes should contain approximately 1–10 linear mesh elements per interface width, with higher contact angles requiring denser meshes. These results are consistent with typical mesh densities used in phase-field or other simulations with varying topologies (Welland et al. 2014).

Comparison against the Gibbs-Thompson effect

In order to demonstrate that the model captures mesoscale effects such as the Gibbs-Thompson effect correctly, simulations were performed varying the initial bubble

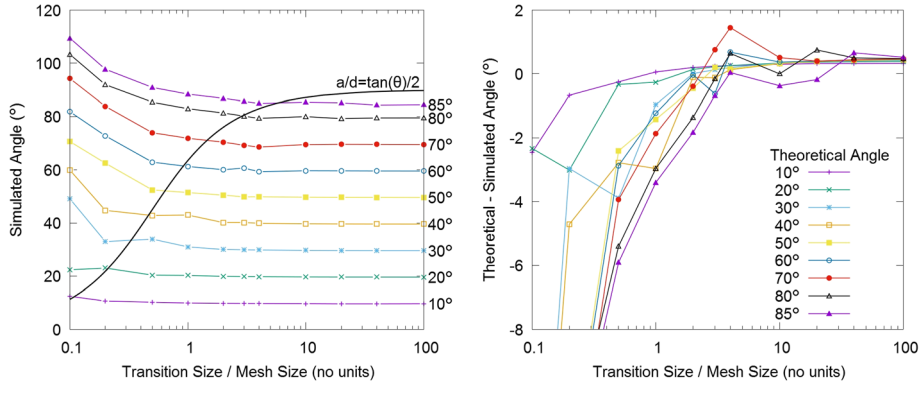

Fig. 11 *Left*: plot of contact angles calculated via the two-point method as a function of the mesh density and theoretical sharp interface angle for a transition size of 0.1 μm. *Right*: difference between the theoretical and simulated contact angles from the figure to the left

radius over several orders of magnitude and determining the equilibrium bubble radius and corresponding chemical potential. Simulations were run using interfacial energies of $\sigma_{\alpha\beta}/\sigma_{\alpha\gamma} = \cos(30°)/2$ and $\sigma_{\beta\gamma} = 0$ which correspond to a contact angle $\theta = 30°$ on a flat surface according to Eq. 50. The classical Gibbs-Thompson theory predicts (Lupis 1983)

$$\mu_r - \mu_\infty = \frac{2\sigma_{\alpha\beta}}{r_{eq}}, \tag{53}$$

where μ_r and μ_∞ are the chemical potentials for a bubble of radius r and a flat interface, respectively. Figure 12 shows the calculated μ_r as a function of the equilibrium bubble radius, along with Eq. 53. As the spatial extent of the simulation is increased by several orders of magnitude, the transition size may be increased accordingly to reduce computational cost; thus, several overlapping datasets are depicted.

It is noted that as $r \to \infty$, $\mu_r \to 0$, implying that the flat interface chemical potential $\mu_\infty = 0$. It should be emphasised here that this does not preclude a standard reference potential but, rather, that this shifts the results uniformly.

The agreement between the simulated μ_r and the corresponding value computed with the analytical solution (i.e. Eq. 53) with $\mu_\infty = 0$ is excellent, implying that the effect of precipitates with high surface curvature modifying the solubility of c in the surrounding material is correctly captured. This effect leads to various coarsening phenomena, along with bubble collapse if energetically unfavourable (Welland et al. 2015b).

Example application to grain boundary porosity in nuclear fuel

As a demonstration of the applicability of the model in 3D, a simulation of the evolution of intergranular porosity in UO_2 nuclear fuel was performed. The initial porosity is controlled as part of the manufacturing processes in which UO_2 powdered compacts are sintered at high temperatures to form solid pellets. The sintering process also continues during fuel irradiation due to a combination of high operational temperatures, radiation fields, and hydrostatic pressure. During operation in-reactor, the grain boundaries accumulate insoluble fission products—such as xenon and krypton—which

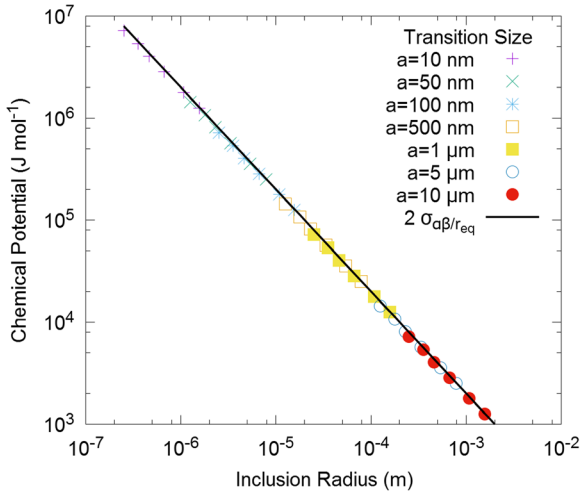

Fig. 12 Plot of predicted mu vs equilibrium bubble radius

pressurise and grow intergranular porosity. The behaviour of these intergranular bubbles is important to fuel performance as they contribute to design limiting phenomena including fuel swelling, degradation of thermal conductivity, and potential releases of fission product inventories. The bubbles grow, coalesce, and percolate along grain faces and grain edges, forming a complex network of tunnels, as shown in Fig. 13 (Ahmed et al. 2016; Rokkam et al. 2009; White and Tucker 1983; Turnbull and Cornell 1971; Jackson and Catlow 1985; White 2001; Pastore 2012). Once a continuous tunnel reaches a crack or the outer surface of a fuel pellet, all the gas in the interconnected tunnel may be vented and the tunnels may collapse.

The intergranular porosity is modelled as phase confined to the grain boundaries of a polycrystalline material. The grain geometry is represented as a truncated octahedron, which is a tetrakaidecahedron with eight regular hexagonal faces and six square faces, that can be tiled infinitely to represent a polycrystalline lattice (White and Tucker 1983). This geometry was constructed from 2D planer surfaces arranged in 3D space to produce the truncated octahedron shape with the focal point, f, at the 3D centre. A grain approximately 15 μm across was meshed with a maximum element size of 0.69 μm, which from Eq. 49 corresponds to five mesh elements per interface width. A total of 31,974 quadrilateral elements in a mapped/structured grid on square faces and 268,546 triangular elements were used on the hexagonal faces. The resulting model contains 332,498 degrees of freedom (DOF). The mesh nodes along the edges are shared between the adjoining faces which enforces continuity of the h field and therefore surface S between the faces.

For comparison, meshing this volume with tetrahedral elements of uniform size with the same maximum size would require approximately 36 million 3D elements and approximately 120 times the DOF. Additionally, the computational expense of the 2D model is lower compared to the 3D model since the 2D finite elements also produce greater matrix sparsity associated with the reduction in dimensionality.

Results of a sample calculation on this grain are provided in Fig. 14, which was initialized with a random initial h field uniformly between 22.6 and 223 nm, equivalent to 7.7% initial intergranular porosity (Additional file 1). These results are based off surface

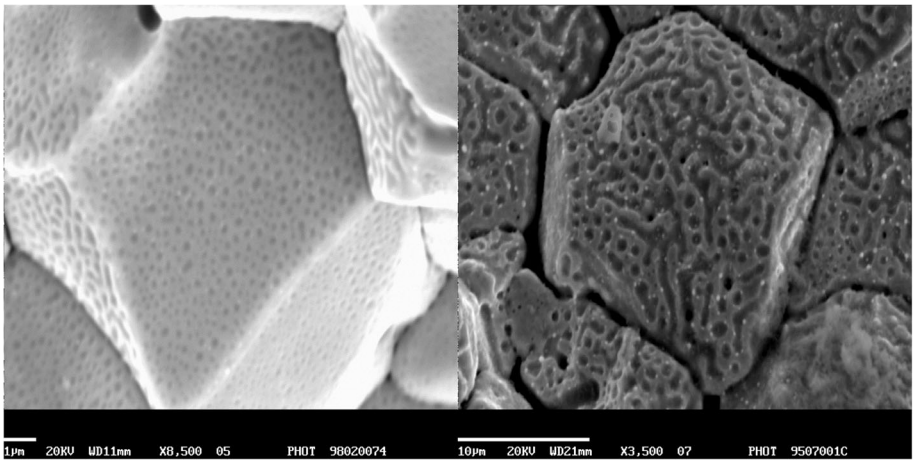

Fig. 13 Example scanning electron microscope images of grain boundary porosity of irradiated nuclear fuels during early stages of formation (*left*) and advanced stages (White 2004; White et al. 2006)

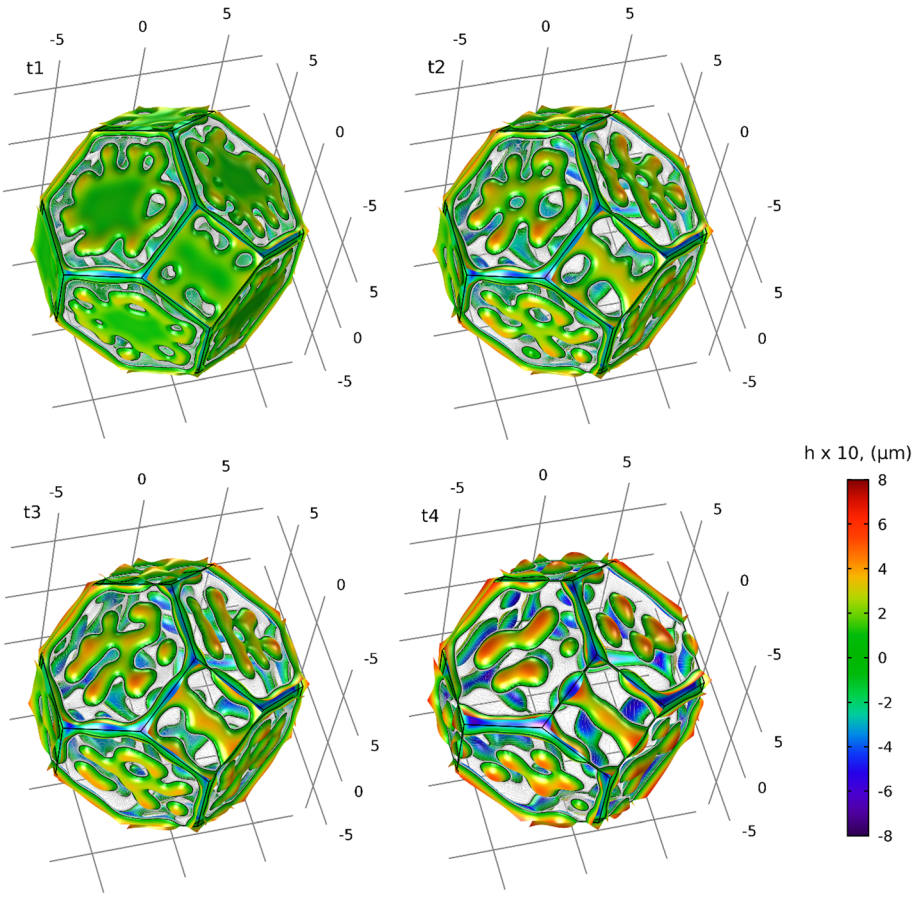

Fig. 14 Results of grain boundary porosity simulation progressing from *top left* to *bottom right* showing decomposition of the initial fluctuating porosity into discrete bubbles followed by interlinkage, coalescence, and relocation towards edges Additional file 1

energies corresponding to a contact of 30° with respect to the computational domain X and a transition size τ of 0.1 μm. The porosity was assumed to be reflected above and below each face, which produced an open bubble section on the grain edges and at the vertices, as seen in Fig. 14.

The timescale in this simulation is arbitrary and depends on the material properties such as orientation-dependent interfacial energies and the surface mobility.

The initial randomly fluctuating porosity rapidly smooths to reduce the surface area and areas of high curvature. The smoothed surfaces then begin to decompose into bubbles with the set contact angle (beading). The phase decomposition begins at the vertices and edges and propagates inwards since these are the lowest energy locations. The bubbles then coarsen and coalesce with the other bubbles nearby.

It is interesting to note that the porosity slowly moves towards the grain boundary edges and vertices, which is energetically favourable due to the increase in interfaces. Edge and vertex adherence is therefore implicitly captured within the model. This phenomenon is observed experimentally in post-irradiation examination of irradiated fuel samples, where rounded prismatic tunnels form along the grain edges (White and Tucker 1983). With sufficient grain edge porosity, these tunnels can form an

interconnected network connecting to macroscopic cracks venting the fission gas accumulated on the grain boundary faces to the free volume.

This simulation result demonstrates preliminarily the applicability of this model to the problem of grain boundary porosity, including prediction of key features, such as bubble coalescence and edge and vertex adherence, in a computationally efficient manner. The use of this work in analysing intergranular porosity in nuclear fuel requires additional physics such as orientation-dependent grain boundary energies and source terms for fission gas. The kinetics of the model could be determined by calibration against experimental data or by including information from lower length-scale calculations.

Discussion

This technique can be applied to study a wide range of phenomena where a phase is confined to an interface between two other phases. In this paper, we have derived the model considering interfacial energies as the only driving force for the evolution of the included phase, although the same methodology can be used to extend to consider many addition effects such as pressure, gravity, temperature gradients, or drag. These effects can be incorporated in one of two ways. First, they can be directly added as volume or surface force terms in Eqs. 21 and 22. This may be appropriate for some relatively simple phenomena where the effect on the species flux is already known. The second method is more general, in that the energy functional in Eq. 3 or 10 is modified to include the energy of the additional phenomena. For example, adding the gravitational potential energy to the functional and propagating the change through the rest of the derivation would produce an additional terms in the chemical potential leading to an additional flux term corresponding to the force of gravity (or buoyancy) on the included phases.

While the technique is versatile and widely applicable, there are important limitations as a result of the projection method. In order for the technique to work, it must be possible to write the potential energy as a function of the position $\vec{x}$, h, and their derivatives (e.g. volume, surface area, or phase) or other variables defined *along the surface* X. Thus, some volumetric effects such as fluid pressure or dissolved species could be included assuming that they do not vary away from the surface. However, it is possible to couple this model of phase inclusions on a 2D surface to another model in the 3D space, potentially on a coarser mesh. An example of this is wind flow around a vehicle moving water droplets on its surface.

The model is able to accommodate moderate motion of S, as long as the relationship between S and $\vec{f}$ is maintained. In order to avoid inverting or producing self-intersection of the surface S, the magnitude h must be less than the distance to the focal point $\vec{f}$ which limits grain growth or movement. Boundary pinning effects due to the inclusions on the surface may also be considered; however, it is not well suited for modelling inclusions above or below the surface and so break-away is not permitted. This is a result of the projection method used to track the interfaces, the mapping must be one to one between X and S. Thus, it only tracks one interface at each point for each variable h. In simple cases, effects from above or below may be captured as source/sink terms in the conservation equation or additional contributions to the

energy functional. For example, diffusion of a species from a grain can become a source term on the grain surface. The diffusion could be solved with a spatially coarser mesh or lower dimensionality model leading to very significant savings. However, if the inside of the grain was already treated with a comparable phase-field model, this surface model might be redundant, introducing additional restrictions and overhead from the projection technique.

In its current formulation, it has been implicitly assumed that X and $\overrightarrow{r}$ are independent of time. However, this assumption could be relaxed allowing for somewhat greater deformation of the computational domain with time. This would require additional care to update the $\overrightarrow{r}$ vector field at each timestep as well as ensuring that the conservation of the included phase is still respected. It is also necessary to maintain the topology of the geometry (boundaries cannot be created or destroyed) or introduce a remeshing/reintialisation step in order to complete the simulation when these changes occur.

This technique is analogous to the use of shell element in modelling solid mechanics. The techniques achieve a reduction in dimensionality by incorporating the response in the out-of-plane directions into the response along the surface. Both techniques are only applicable to a subset of problems; however, where they are applicable, they can result in very substantial reductions in computational costs.

Conclusions

The current work develops a model for the behaviour of inclusions on the boundary between two phases, exploiting a projection technique to reduce the dimensionality of the problem and thus significantly reduce computational expense by a factor proportional to the ratio of volume to surface area (compared to a uniform volume mesh). These gains are offset slightly by the additional assembly overhead needed for the projection. The full model and several simplifications were derived. The properties of the solution were analysed and characterised. The model is shown to capture mesoscale effects that lead to coarsening and reproduction of the Gibbs-Thompson effect. An example model of grain boundary porosity is shown, which captures the phenomena of intergranular porosity interlinkage and migration towards edges.

Additional file

Additional file 1: Results of grain boundary porosity simulation showing decomposition of the initial fluctuating porosity into discrete bubbles followed by coalescence and relocation towards edges and vertices. (MP4 8067 kb)

Acknowledgements
The authors would like to thank Jacob Siemons for several helpful discussions.

Authors' contributions
The authors declare that they contributed equally to this work in all aspects. Both authors read and approved the final manuscript.

Competing interests
The authors declare that they have no competing interests.

Publisher's Note

Received: 23 December 2016 Accepted: 30 March 2017
Published online: 25 May 2017

References

K Ahmed, T Allen, A El-Azab, J. Mater. Sci. **51**, 1261–1277 (2016)
JW Cahn, JE Hilliard, J. Chem. Phys. **28**, 258 (1958)
P Chakraborty, MR Tonks, G Pastore, J. Nucl. Mater. **452**, 95–101 (2014)
A Choudhury, B Nestler, Phys. Rev. E 85 (2012).
J Donea, A Huerta, J-P Ponthot, A Rodríguez-Ferran, in *Encycl. Comput. Mech.* ed. by E Stein, R de Borst, TJR Hughes (John Wiley & Sons, Ltd, Chichester, UK, 2004)
J Harris, H Stöcker, *Handbook of mathematics and computational science* (Springer, New York, 1998)
LF He, B Valderrama, A-R Hassan, J Yu, M Gupta, J Pakarinen, HB Henderson, J Gan, MA Kirk, AT Nelson, MV Manuel, A El-Azab, TR Allen, J. Nucl. Mater. **456**, 125–132 (2015)
RA Jackson, CRA Catlow, J. Nucl. Mater. **127**, 161–166 (1985)
Y Li, J Kim, Int. J. Heat Mass Transf. **55**, 7926–7932 (2012)
CHP Lupis, *Chemical thermodynamics of materials* (North-Holland, New York, 1983)
B Nestler, H Garcke, B Stinner, Phys. Rev. E **71**, 041609 (2005). doi:10.1103/PhysRevE.71.041609
G Pastore, *Modelling of fission gas swelling and release in oxide nuclear fuel and application to the TRANSURANUS Code, Politecnico Di Milano*, 2012
N Provatas, M Greenwood, B Athreya, N Goldenfeld, J Dantzig, Int. J. Mod. Phys. B **19**, 4525–4565 (2005)
S Rokkam, A El-Azab, P Millett, D Wolf, Model. Simul. Mater. Sci. Eng. **17**, 064002 (2009)
JA Turnbull, RM Cornell, J. Nucl. Mater. **41**, 156–160 (1971)
MJ Welland, in Comprehensive Nuclear Materials, 1st edn, ed. by RJM Konings (Elsevier, Oxford, 2012), p. 629–676.
MJ Welland, D Wolf, J.E. Guyer, Phys. Rev. E 89 (2014).
MJ Welland, D Karpeyev, DT O'Connor, O Heinonen, ACS Nano **9**, 9757–9771 (2015a)
MJ Welland, KC Lau, PC Redfern, L Liang, D Zhai, D Wolf, LA Curtiss, J. Chem. Phys. **143**, 224113 (2015b)
RJ White, J. Nucl. Mater. **295**, 133–148 (2001)
RJ White, J. Nucl. Mater. **325**, 61–77 (2004)
RJ White, MO Tucker, J. Nucl. Mater. **118**, 1–38 (1983)
RJ White, RC Corcoran, PJ Barnes, *IFPE/CAGR-UOX-SWELL fuel swelling data obtained from the AGR/Halden Ramp Test Programme, Organization for Economic Cooperation and Development Nuclear Energy Agency, Paris, France*, 2006